Published in : Acta Biomaterialia (2023), vol. 166, pp. 409–418
DOI: 10.1016/j.actbio.2023.04.018
Status : Postprint (Author's version)

STRUCTURAL AND FUNCTIONAL HETEROGENEITY OF MINERALIZED FIBROCARTILAGE AT THE ACHILLES TENDON-BONE INSERTION

Alexandra Titsa, Stéphane Blouinb, Maximilian Rummlerc, Jean-François Kauxd, Pierre Drion e, G. Harry van Lenthef, Richard Weinkamerc, Markus A. Hartmannb, Davide Ruffonia,*

[a] *Mechanics of Biological and Bioinspired Materials Laboratory, Department of Aerospace and Mechanical Engineering, University of Liège, Liège, Belgium*

[b] *Ludwig Boltzmann Institute of Osteology at Hanusch Hospital of OEGK and AUVA Trauma Centre Meidling, 1st Medical Department Hanusch Hospital,*

Vienna, Austria

[c] *Department of Biomaterials, Max Planck Institute of Colloids and Interfaces, 14476 Potsdam, Germany*

[d] *Department of Physical Medicine and Sports Traumatology, University of Liège and University Hospital of Liège, Liège, Belgium*

[e] *Experimental Surgery unit, GIGA & Credec, University of Liège, Liège, Belgium*

[f] *Department of Mechanical Engineering, KU Leuven, Leuven, Belgium*

**Corresponding author at: Department of Aerospace and Mechanical Engineering, University of Liège, Quartier Polytech 1, Allée de la Découverte 9, B-4000 Liège, Belgium*

Keywords:

Enthesi, Mineralized fibrocartilage, Nanoindentation, Quantitative backscattered electron imaging, Second harmonic generation imaging

Abstract

A demanding task of the musculoskeletal system is the attachment of tendon to bone at entheses. This region often presents a thin layer of fibrocartilage (FC), mineralized close to the bone and unmineralized close to the tendon. Mineralized FC deserves increased attention, owing to its crucial anchoring task and involvement in enthesis pathologies. Here, we analyzed mineralized FC and subchondral bone at the Achilles tendon-bone insertion of rats. This location features enthesis FC anchoring tendon to bone and sustaining tensile loads, and periosteal FC facilitating bone-tendon sliding with accompanying compressive and shear forces. Using a correlative multimodal investigation, we evaluated potential specificities in mineral content, fiber organization and mechanical properties of enthesis and periosteal FC. Both tissues had a lower degree of mineralization than subchondral bone, yet used the available mineral very efficiently: for the same local mineral content, they had higher stiffness and hardness than bone. We found that enthesis FC was characterized by highly aligned mineralized collagen fibers even far away from the attachment region, whereas periosteal FC had a rich variety of fiber arrangements. Except for an initial steep spatial gradient between unmineralized and mineralized FC, local mechanical properties were surprisingly uniform inside enthesis FC while a modulation in stiffness, independent from mineral content, was observed in periosteal FC. We interpreted these different structure-property relationships as a demonstration of the high versatility of FC, providing high strength at the insertion (to resist tensile loading) and a gradual compliance at the periosteal surface (to resist contact stresses).

Statement of significance

Mineralized fibrocartilage (FC) at entheses facilitates the integration of tendon in bone, two strongly dissimilar tissues. We focus on the structure-function relationships of two types of mineralized FC, enthesis and periosteal, which have clearly distinct mechanical demands. By investigating them with multiple high-resolution methods in a correlative manner, we demonstrate differences in fiber architecture and mechanical properties between the two tissues, indicative of their mechanical roles. Our results are relevant both from a medical viewpoint, targeting a clinically relevant location, as well as from a material science perspective, identifying FC as high-performance versatile composite.

1. Introduction

Cartilage is a highly versatile tissue essential to the functioning of the musculoskeletal system. Articular (hyaline) cartilage and fibrocartilage (FC) are two types of cartilage present in mammals, which share the same constituents but in different proportions and arrangements depending on the anatomical location and mechanical function [1]. Cartilage is found at mechanically challenging locations to cope with tasks that bone alone cannot solve. The ends of the bones that articulates in a joint, for example, are covered by a layer of unmineralized articular cartilage, followed by a thin region of mineralized cartilage, and then subchondral bone. Thanks to a sophisticated interplay between extracellular matrix and water, combined with consecutive layers of varying collagen orientation, the millimeter-thick unmineralized articular cartilage provides lubrication and resistance to contact stresses [2]. At the same time, with only a few hundreds of micrometers in thickness, mineralized cartilage must ensure a proper anchoring between cartilage and bone [3]. Similarly, at the insertion of tendons and ligaments into bone, particularly when the insertion angle changes considerably during joint movement, FC is present [4]. This integrative tissue is also found at meniscal attachment to bone [5–7]. In analogy with articular cartilage, FC comes in two forms: unmineralized FC (uFC) close to tendon/ligament and mineralized FC (mFC) close to bone. Like bone and tendon, FC is a highly fibrous tissue but composed of a mixture of collagen type II and III (rather than collagen type I) and proteoglycans [8,9]. In mFC, the fibrous matrix gets reinforced by mineral crystals and anchors to bone [10]. Knowing that bimaterial attachments are at risk of stress localization [11], the interface between uFC and mFC is considered the weakest link in the force transmission from tendon to bone, and it has received considerable attention. A fine tuning of composition and hierarchical organization across the interface provides enthesis with high mechanical efficiency, allowing the transmission of large forces for many years

[9,12–15]. mFC away from the interface and even the underlying (subchondral) bone have been investigated less. This is unfortunate as these regions may also be the cause of attachment failure, especially following a (high) monotonic loading event [16] or when the physiological loading conditions are altered [17]. Furthermore, studies on articular cartilage have underlined key structure-property relationships contributing to anchoring cartilage to bone [3,18–20].

In this work, we exploited high-resolution material characterization methods to detect the effect of mechanical loading on the structure and mechanical properties of mFC at the micrometer length scale. Specifically, we analyzed the Achilles tendon-calcaneus bone enthesis in rats, one of the most used animal model to investigate enthesis diseases [21,22] and the musculoskeletal system in general, especially tendons [23,24], given its similarities with humans. Two types of FC can be found there, each with different mechanical loading conditions: enthesis FC anchors tendon to bone, therefore sustains predominantly tensile loads, whereas periosteal FC facilitates tendon sliding and bone-tendon contact with accompanying compressive and shear forces. In a previous work, we highlighted a strong anisotropy of the microstructural porosity (fibrochondrocyte lacunae and channel network) within enthesis mFC (E-mFC), with pores strongly oriented towards the tendon insertion [25]. Here, we combine nanoindentation with quantitative backscattered electron imaging (qBEI) and second harmonic generation (SHG) imaging on the exact same locations. As biological tissues have locally varying composition and microstructural organization, which are particularly pronounced at the connection between tendon and bone, our approach is to spatially correlate mechanical properties with mineral content and matrix organization. We assume this is a necessary step to elucidate the structure-property relationship of such a heterogeneous multi-tissue region. On the top of this, we also consider both longitudinal and transverse directions to address the inherent anisotropy of the tissue.

2. Materials and methods

2.1. SAMPLE PREPARATION

Achilles tendon-calcaneus bone samples (*n* = 3) were extracted from the posterior legs of three 3-month-old male Sprague-Dawley rats (weight of 402 ± 31.2 g) and stored in 70% ethanol. Animals were available at the Liège University Hospital in the framework of an organ donation program (ethical approval: ULg-IACUC-21–2340). Samples were prepared to expose representative cross-sections of the tendon-bone insertion. Following dehydration and embedding in polymethyl methacrylate (PMMA), samples were cut along the sagittal plane with a diamond saw (Buehler Isomet 1000), using the calcaneal tuberosity as a visual guidance for sample positioning (**Fig. S1**). Sample surface was ground with sand-paper until the tendon-bone insertion at the calcaneal tuberosity was spotted. A final polishing step using a diamond suspension (grain size down to 1 µm, Logitech PM5) completed the sample preparation. After performing qBEI, SHG imaging and biomechanical analysis on the sagittal sections, two samples were cut along the transverse plane and polished, such that two-mutually perpendicular cross-sections could be characterized for each sample.

Published in : Acta Biomaterialia (2023), vol. 166, pp. 409–418
DOI: 10.1016/j.actbio.2023.04.018
Status : Postprint (Author's version)

2.2. QUANTITATIVE BACKSCATTERED ELECTRON IMAGING

To quantify the mineral content, qBEI [26] was performed on carbon-coated samples ($n = 3$) with a Field Emission Scanning Electron Microscope (FESEM, Supra40, Zeiss) [27]. The measurements were performed at 20 kV with a working distance of 10 mm and a scan speed of 90 s per frame [27]. Images were acquired at a magnification of 130x, yielding a nominal isotropic pixel size of 0.88 µm, and considering a 1024 × 768 pixel window. By stitching together adjacent measurements recorded with a 5% spatial overlap, the entire sample surface was characterized. The intensity of the electrons backscattered from a thin (i.e., about 1–2 µm in thickness) surface layer is mainly determined by the local calcium concentration [26]. To allow a quantitative assessment of calcium content, the FESEM was calibrated with carbon and aluminum standards according to a previously established procedure [26]. The gray values of the reference materials were set to 25 and 225, respectively. These settings led to gray values of 25 for osteoid (0 wt% Ca) and 255 for pure hydroxyapatite (39.86 wt% Ca). This allowed to translate the gray level (GL) images into spatial maps of the mineral content expressed as calcium weight percentage via [26]:

$$\text{Ca [wt\%]} = -4.332 + 0.1733 \times \text{GL} \quad (1)$$

Before further quantification, the following pre-processing steps were performed with the software CTAn (v1.19.4.0, Skyscan). First, bone and mFC were manually segmented following the interface between the two tissues (see black dashed line in **Fig. 1**). To minimize boundary effects [28], a 1 pixel erosion operator was applied. Signals from the embedding resin and non-mineralized tissues were removed by setting a minimum threshold for the mineral content (5.2 wt%). Individual unconnected pixels were also discarded. The mineralization maps highlighted the presence of several highly mineralized regions, especially in the trabecular compartment (**Fig. S3**). In a previous work, we have shown that these are cartilaginous inclusions of high mineral content [25], which have been also observed in rat cortical bone [29,30]. The highly mineralized islands were discarded from the present analysis by setting an upper threshold of 29.5 wt% (determined by visual inspection). The mineralization maps were then summarized into mineralization density frequency distributions and normalized to unit area. The following five parameters were introduced to characterize the resulting histograms [28]: Ca_{mean} (average Ca concentration), Ca_{peak} (most frequent Ca concentration), Ca_{width} (full width at half maximum), Ca_{low} and Ca_{high}. The last two parameters describe the amount of low and high mineralized regions, corresponding to areas mineralized below the 5th percentile and above the 95th percentile of a reference distribution. Here, the histogram of subchondral bone adjacent to mFC was taken as reference, with $\text{Ca}_{\text{low}} = 22$ and $\text{Ca}_{\text{high}} = 27$ wt%. These values were then used to compute the area below Ca_{low} and above Ca_{high} on mFC distributions.

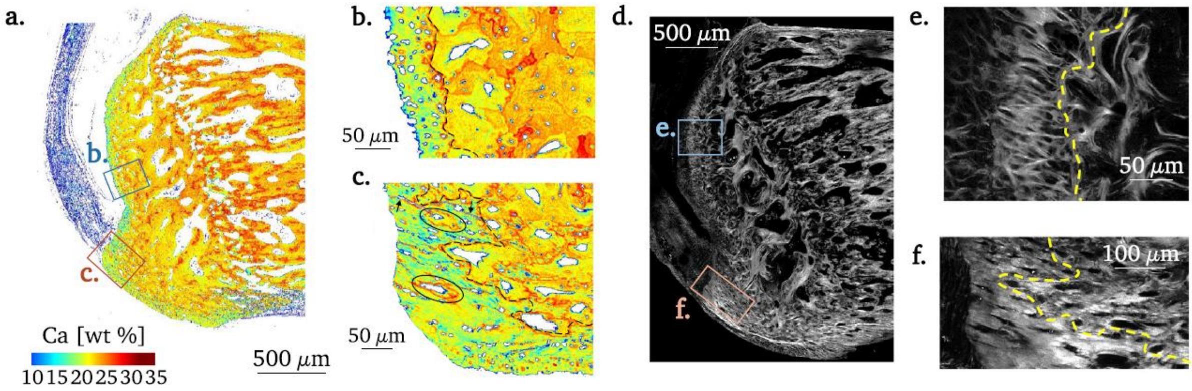

Fig. 1. (a) Mineralization pattern from quantitative backscattered electron imaging (qBEI) and (d) corresponding fiber organization from second harmonic generation (SHG) imaging. Magnified views of qBEI data at (b) periosteal and (c) enthesis regions. Black dashed lines indicate the interface between mineralized fibrocartilage (mFC) and bone used to segment the different regions. Black closed lines (ellipse shaped) denote bone regions fully encircled by mFC, and arrows emphasize long cracks entering E-mFC. Magnified views of SHG images highlighting the specificities of (e) periosteal and (f) enthesis locations. The yellow dashed line represents the interface between mFC and bone, detected by superimposing SHG and qBEI images.

2.3. SECOND HARMONIC IMAGING

To visualize the arrangement of collagen fibrils, SHG imaging [31,32] was used and we considered the polished samples which clearly showed the tuberosity in the qBEI maps (n = 2). In this nonlinear light scattering process, a strong SHG signal is usually generated by regions with densely packed collagen fibrils, preferentially arranged parallel to the imaging plane. Conversely, if collagen fibrils are oriented out of the image plane, no signal should be detected [33–35]. In between these two scenarios, intermediate intensities are measured depending on several factors including collagen charge density and out-of-plane orientation. Second harmonic imaging was performed using a SP8 confocal microscope (Leica Microsystems, Wetzlar, Germany) with a 40x oil immersion objective (HC PL APO 40 × /1.30 OIL) without using the pinhole, corresponding to a nominal isotropic pixel size of 379 nm. A Mai-Tai high performance Ti:Sa Laser (Spectra-Physics, Milpitas, CA, USA) operating in pulse mode at a wavelength of 910 nm was used, and the backward direction signal was detected at 450–460 nm. Several windows of 1024 × 1024 pixels were analyzed and stitched together such that exactly the same regions were characterized by both qBEI and SHG.

2.4. NANOINDENTATION AND DATA PROCESSING

The polished PMMA-embedded samples showing the tuberosity (n = 2) were mechanically characterized by nanoindentation (Triboindenter TI 950, Bruker, US) to measure indentation modulus and hardness. The nanoindenter was equipped with a Berkovich diamond probe (50 nm tip radius) and a displacement controlled trapezoidal load function was used (8–20–8 s), with a maximum displacement of 500 nm. The average surface roughness of the mineralized tissues, measured by scanning 20 µm x 20 µm regions with the tip of the nanoindenter at 2 µN contact force, was 15.5 ± 6.7 nm. The indentation depth was well above the recommended threshold of 10 times the surface roughness [36,37].

Due to inelastic deformation, the lateral spacing between indents should be at least three times the contact radius [19], or 4.2 µm in our setting. A spacing of 6 µm was chosen here and several indentation grids (for a total of about 3000 indents) were performed on regions across the bone-mFC interface, selected on both enthesis and periosteal areas with the help of the qBEI maps (**Fig. S4**). The probe contact area was calibrated with fused quartz and the obtained load-depth curves were analyzed with the Oliver-Pharr method [38], to extract indentation hardness (H) and reduced modulus (Er). The nanoindentation grids were then super-imposed on the qBEI maps through a manual registration procedure. This allowed to classify indents as belonging to mFC or bone, as well as to discard indents falling within cracks or holes (**Fig. S4**). When performing nanoindentation we tried to avoid the highly mineralized cartilaginous inclusions; nevertheless, the superimposition of the nanoindentation grids with the qBEI images revealed that some indents (less than 1%) were placed inside the cartilaginous regions, which are known to be 10 – 25% stiffer than surrounding bone [30] and hence they were discarded from the analysis. To correlate the mineral content with the local mechanical properties (Er and H), the calcium concentration was averaged over a 4 × 4 pixel region centered around each indent. This size can be considered representative of the elastic field probed by the indent at 500 µm depth [19]. To assess the spatial evolution of the mechanical properties when entering the mineralized tissues, the shortest distance (Euclidean) of each indent from the mineralized surface was computed (**Fig. S4**). In soft tissues, especially close to the interface with mineralized tissues, only a limited number of indents could be considered due to higher roughness. As for the mineral content, histograms of reduced modulus and hardness were calculated and characterized by similar parameters. Low and high values for elastic modulus and hardness were calculated considering the corresponding distributions of subchondral bone (i.e., $E_{r,\,low}$ = 17.5 and $E_{r,\,high}$ = 25.4 GPa; H_{low} = 0.55 and H_{high} 0.79 GPa) and were used for calculating areas below these limits on the mFC distributions.

2.5. STATISTICAL METHODS

We used statistical analysis for two purposes: to compare the mean mineralization needed to reach specific tissue modulus and hardness values (**Fig. 3**b and **S8**d) as well as to compare properties between sagittal and transverse sections (**Fig. 6**). We applied a two-sample Student's *t*-test with normality checked by a Kolmogorov-Smirnov test and homoscedasticity by a two-sample F-test. If one of those criteria was not met, a Mann-Whitney *U test* was employed. P-values smaller than 0.05 were considered significant. Mechanical properties-mineral content relationships were evaluated with a two-parameter exponential model and nonlinear regression was used to determine the values of the parameters. The statistical analysis was performed in Matlab (statistics toolbox) [39] and SigmaPlot (nonlinear regressions).

3. Results

3.1. QUALITATIVE OBSERVATIONS ON MINERAL CONTENT AND FIBER ORGANIZATION

Before entering into the quantification of tissue properties, a qualitative observation of the qBEI images already highlights several features of the mineralization pattern. The layer of mFC at both periosteal and insertion sites is often demarcated from bone by a thin, very irregular and highly mineralized interphase which, in analogy with the interphase bordering osteons, is named cement line (dashed black line in **Fig. 1**b, c). Some regions of bone containing osteocyte lacunae appear as fully encircled by mFC even several tens of micrometers away from the interface (highlighted by closed lines **Fig. 1**c and **Fig. S6**a). These isolated bone "islands" in 2D sections are possibly interconnected in 3D and linked to the rest of the bone, allowing access to nutrients. Therefore, the connection between mFC and bone should be highly interdigitated. As qBEI provides only 2D information, the visualization of the complex interdigitations in 3D could be obtained using synchrotron radiation computed tomography. At the insertion site, the mFC layer is thicker and shows bigger interdigitations than at the periosteal side (also shown for the other samples in **Fig. S5**). The interface between uFC and mFC is also fairly rough, but at a smaller length scale, with interface roughness dominated by arrested fibrochondrocytes and by the irregular mineralization front. Overall, mFC exhibits high porosity at the micrometer length scale due to numerous fibrochondrocyte lacunae, in agreement with a previous investigation [25]. In some locations, former tidemarks, indicating previous interfaces between uFC and mFC [18,40], are detectable (see arrows in **Fig. S6**b).

SHG images provide qualitative insights into fiber organization. Similar to mineralization, an overall heterogeneity is observed (**Fig. 1**d and **S7**). At the insertion and especially towards the inferior side of the tuberosity (**Fig. 1**f), the SHG signal is very strong and rather uniform, suggesting highly aligned (in-plane) collagen fibers, connecting almost continuously the Achilles tendon with the plantar fascia, attaching on the opposite side of the tuberosity. In contrast, periosteal mFC (P-mFC, **Fig. 1**e) shows a more heterogeneous SHG signal with fibers appearing interwoven and following a tortuous path around the many pores present there, somewhat resembling tree roots. At the interface between mFC and bone (highlighted by the dashed yellow line in **Fig. 1**e, f), a continuous fiber arrangement is observed at the insertion site (**Fig. 1**f). Conversely, at the periosteal region, fibers of mFC tend to reach the interface at an almost right angle, whereas (some) fibers from the bone side are oriented parallel to the interface and follow the cement line (**Fig. 1**e). Overall, the SHG signal in bone is markedly different from mFC: thick regions of lamellar bone are recognizable, whereas other areas show a more diffuse signal (**Fig. S3**), indicating less ordered endochondral bone.

3.2. QUANTITATIVE GLOBAL ASSESSMENT OF MINERAL CONTENT AND BIOMECHANICAL PROPERTIES

Quantitative global assessment of mineral content, reduced modulus and hardness are introduced here through the analysis of box-plots and frequency distributions, computed within three different regions of interest: E-mFC, P-mFC and subchondral bone (**Fig. 2**, **S2** and corresponding parameters in **Tables S1**, **S2**). Considering the different spatial resolutions of qBEI and nIND, for a "fair" comparison between mineralization and mechanical properties distributions, histograms of calcium content (**Fig. 2**) were based on average values around indents (distributions from the entire regions can be found in **Fig. S2**). All distributions were peak-shaped and, at least for the calcium content, this is a direct consequence of the interplay between bone mineralization and remodeling [41]. Of high interest is that both E-mFC and P-mFC have mineralization distributions shifted towards lower mineral content with respect to subchondral bone (**Fig. 2**a), reflected in a decrease in Ca_{mean} of ~10% for both mFC. In agreement with a lower mineral content, the frequency distribution of reduced modulus (**Fig. 2**b) and hardness (**Fig. 2**c) are also shifted towards lower values, indicating that E-mFC and P-mFC are less stiff and hard than subchondral bone, with higher differences observed in reduced modulus (decrease in $E_{r,\ mean}$ of ~20% and in H_{mean} of ~8% for both types of mFC). While mineralization distributions of E-mFC and P-mFC are very similar, some differences are present in the distributions of the mechanical properties: the frequency distribution of reduced modulus of E-mFC is characterized by a higher and narrower peak with respect to P-mFC.

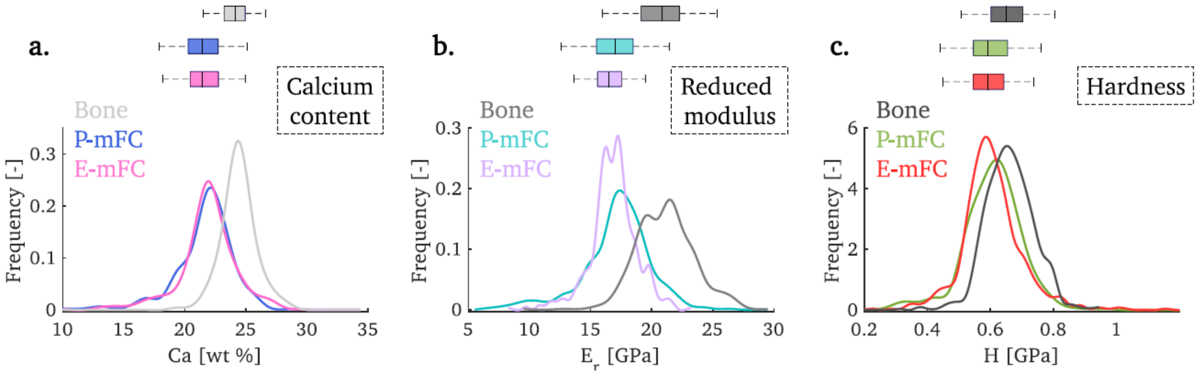

Fig. 2. Frequency distributions and box plot representations of (a) calcium content, (b) reduced modulus and (c) hardness according to tissue type and location. Distributions shown as smoothed splines considering all indentation points on sagittal sections. Boxes range from the 25th to the 75th percentiles, and the vertical line represents the mean value. Whiskers extend to one interquartile away from the box.

3.3. RELATIONSHIP BETWEEN MINERAL CONTENT AND MECHANICAL PROPERTIES

The degree of mineralization is associated with mechanical properties in **Fig. 3**. Despite the increased scatter, calcium content is an important variable in explaining the variations in tissue modulus (**Fig. 3**a) and in hardness (**Fig. S8**c), as confirmed by the two-parameter exponential fit (**Table S3**). In **Fig. 3**b the reduced modulus was binned in the range 14–24 GPa (bin width of 2 GPa), and the corresponding average calcium required to reach each specific elastic modulus was computed. Statistical comparisons of calcium content within each bin reveals that subchondral bone requires a slightly higher mineral content than mFC to reach a specific stiffness level (a similar behavior is observed for hardness, **Fig. S8**d). No difference is present when comparing the two FCs. This is a central finding on the composition-mechanical property relations of the analyzed tissues. Our results can be further interpreted considering a staggered model for mineral packing in an organic matrix as proposed by Jäger and Fratzl [42] (see Supplementary Material), and previously used also to investigate mineralized cartilage [18,43]. The model provides a functional relationship between tissue elastic modulus and mineral content (expressed as mineral volume fraction), allowing to explore the role of different parameters, such the aspect ratio of mineral crystals (ρ in **Fig. 3**a). The model indicates that subchondral bone and mFC, although having different mineral content and organic matrix, lie on similar contour lines.

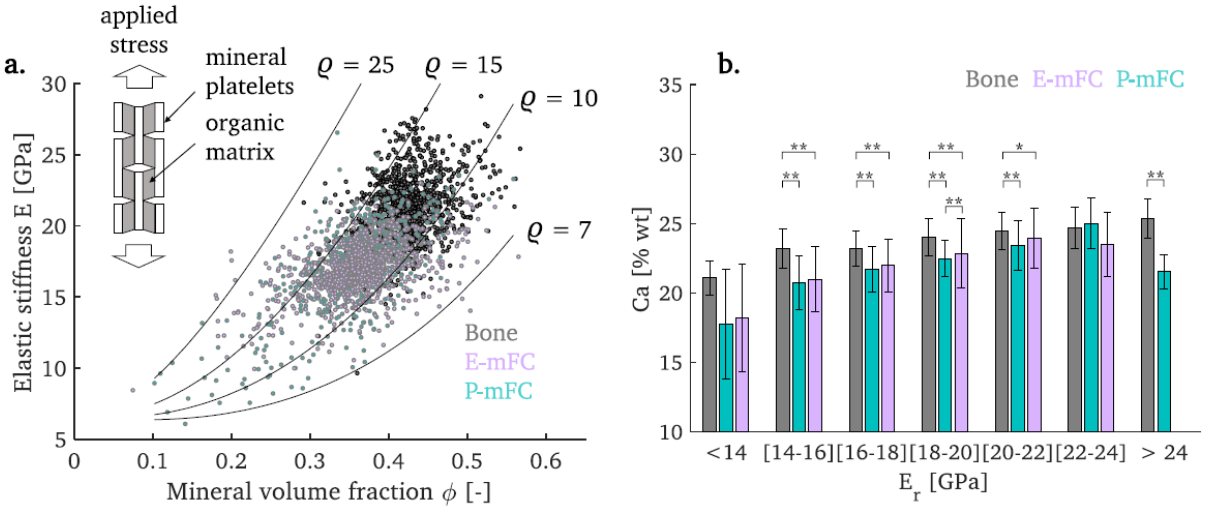

Fig. 3. (a) Experimental modulus-mineral volume fraction relations (all indents are pooled) and comparison with predictions of a staggered model (contour lines) as a function of the mineral platelets aspect ratio *ρ* [18,42]. The schematic represents the staggered model, where an applied external stress induces shear stresses which are transferred from the gray organic matrix to the white mineral platelets. (b) Averaged calcium content values for mFC and bone providing reduced moduli ranging from 14 to 24 GPa. ** $P < 0.01$, * $P < 0.05$.

3.4. MINERALIZATION GRADIENTS ACROSS THE UNMINERALIZED-MINERALIZED INTERFACE

To characterize the local gradients in mineral content across the unmineralized-mineralized interface, the high resolution of qBEI images (i.e. ~0.88 µm pixel size) was exploited. The spatial variation of calcium content measured along several probed lines perpendicular to the interface was fitted with a sigmoid function (**Table S4**). Based on the fitting function, the transition width was defined as the difference between 0.5% and 99.5% height.

As illustrated in **Fig. 4**, the interface between unmineralized and mineralized tissues in both FCs exhibits a gradual increase in mineralization, occurring over a ~14 µm width transition region. In comparison, when entering bone from resin (avoiding regions of low mineral content, probably indicating active modeling site), a much steeper gradient is found, i.e. transition width of ~7 µm. Moreover, the plateau values of the sigmoid away from the interface are very similar in the two FCs (21.3 wt% and 21.4 wt% at enthesis and periosteal regions) and are about 18% lower than in bone (25.3 wt%).

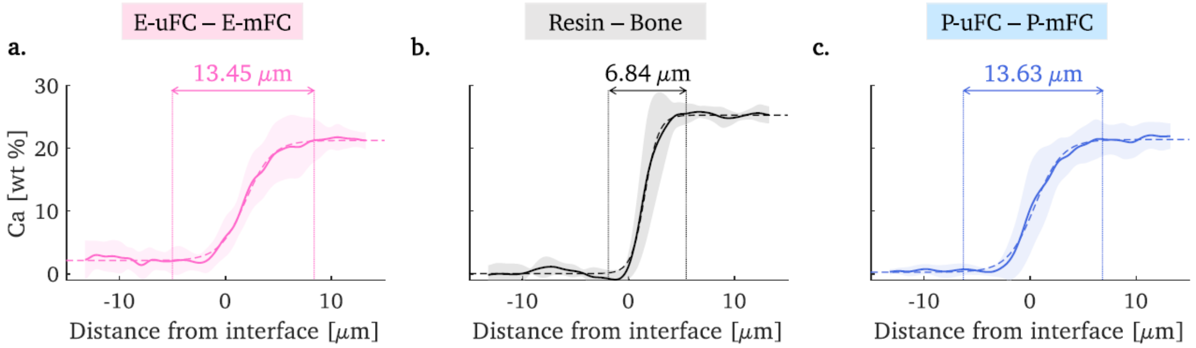

Fig. 4. Spatial evolution of calcium content when entering mineralized tissues from unmineralized regions. (a) Transition from enthesis unmineralized FC (E-uFC) to enthesis mFC (E-mFC). (b) Transition from resin to bone (no FC is present here). (c) Transition from periosteal unmineralized FC (P-uFC) to periosteal mFC (P-mFC). Data shown as average (thick line) and standard deviation interval (shaded areas) over 10 profile lines per region, with the sigmoid fit (dashed line) and corresponding transition width.

3. 5. SPATIAL ANALYSIS OF MINERAL CONTENT, FIBER ORGANIZATION AND MECHANICAL PROPERTIES

To gain further insight into the structure-function relationship of mFC, compositional (qBEI) and mechanical (nanoindentation) data were plotted as a function of the distance from uFC, spanning the entire thickness of the mFC layer and reaching subchondral bone (**Fig. 5** and **S8**a, b). We first present some representative indentation lines, which are interpreted with the help of qBEI and SHG maps of the very same locations (**Fig. 5**a-d). At the insertion (**Fig. 5**a, b), the probed regions typically show a strong and uniform SHG signal: in this case, the reduced modulus follows calcium content very closely and, within E-mFC, a flat profile of both Ca and Er is observed. Conversely, at P-mFC (**Fig. 5**c, d) the SHG is highly heterogeneous, highlighting a complex interwoven fiber arrangement. Although mineral content profiles are rather flat, an unexpected gradual increase in elastic modulus spanning the entire P-mFC region is detected. By pooling all individual measurements (approximately 3000 indents), despite the rather large scatter, one main and evident feature is the practically constant mineral content and modulus profiles within E-mFC (**Fig. 5**e, f), which differ from the gradual increase in reduced modulus observed at the periosteal region (**Fig. 5**g, h). A linear regression of the Er-distance relationship in P-mFC highlights a slope of about 60 MPa/µm. A qualitative similar trend is observed for hardness (**Fig. S8**a, b). The irregular mFC-bone interface has an impact on these plots, as points from bone and mFC have some overlapping, especially at the enthesis, where long "fingers" of bone enter mFC.

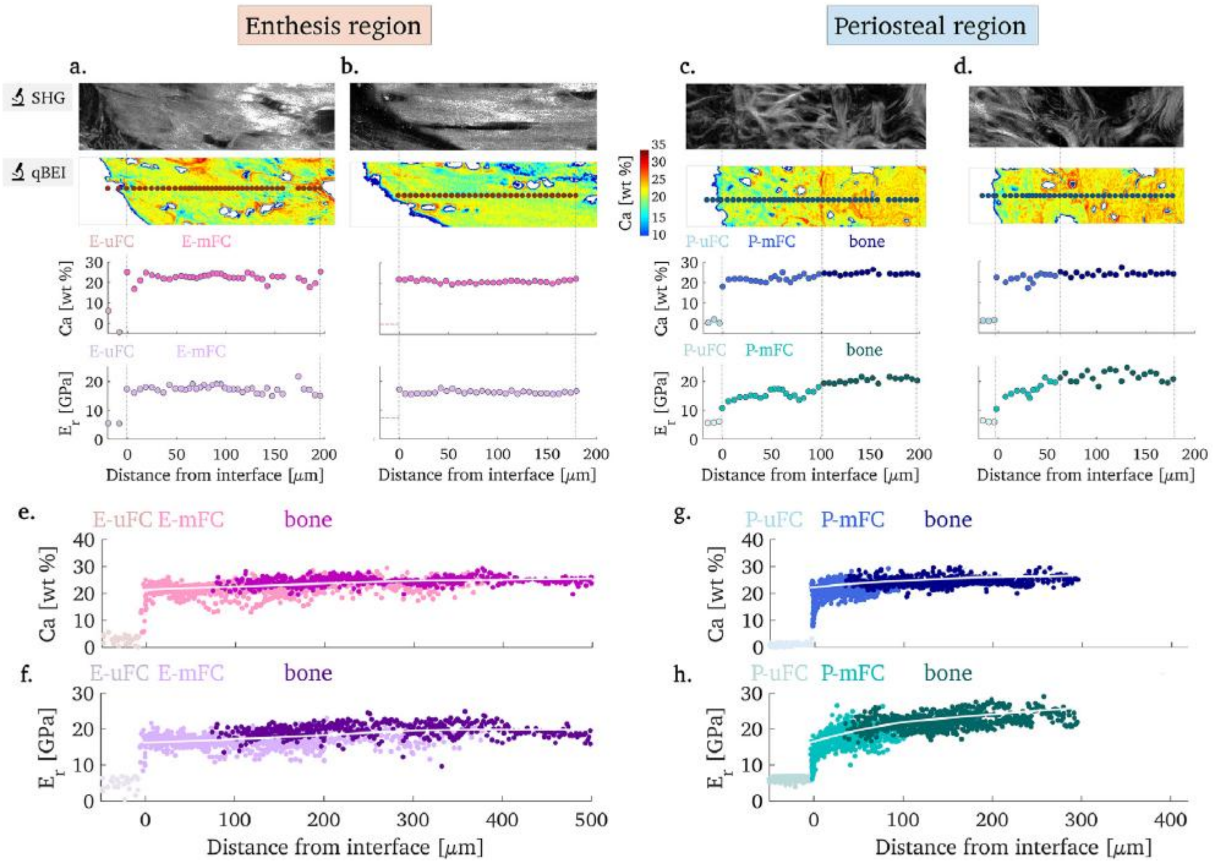

Fig. 5. Spatial modulation of mineral content, fiber organization and mechanical properties. SHG signal, region-matching qBEI maps and representative line scans of calcium content (Ca) and reduced modulus (E_r), measured along the dotted line shown on qBEI maps at (a, b) E-mFC and (c, d) P-mFC. Evolution of Ca and Er for all measured points as a function of the distance from the interface between uFC and mFC. Locally weighted scatter plot smoothing (LOWESS) lines help to visualize the trends (smoothing factor of 0.8).

3.6. ORTHOGONAL SECTION AND THREE-DIMENSIONAL IMPLICATIONS OF STRUCTURAL ANISOTROPY

An orthogonal section (perpendicular to the already analyzed sagittal planes) was exploited to investigate material anisotropy at the enthesis. To a first approximation, in sagittal sections, mineralized collagen fibers lie parallel to the analyzed surface meaning that nanoindentation is performed along the transverse axis of the fibers. The opposite is true for the orthogonal section, which exposes fibers roughly perpendicular to the analyzed surface, thus being tested along their longitudinal axis. As illustrated in **Fig. 6**, E-mFC has a highly heterogeneous and location-specific mineralization pattern, with higher mineral content observed in the central regions anchoring the tendon (visible in the sagittal section) in comparison to the periphery of the attachment (visible in the transverse section). The corresponding frequency distributions of mineral content are reported and quantified in **Fig. S9**. SHG images reveal how a strong signal in the sagittal section, indicating highly aligned fibers, becomes a very weak signal in the adjacent transverse plane, confirming that the fibers are now oriented perpendicular to the imaging section. Several indents ($n = 21$) placed inside mFC on virtually the same locations but belonging to the two orthogonal planes highlight the anisotropic biomechanical character of mFC at the enthesis: higher modulus (10.7%, $p < 0.01$) and hardness (6.3%,

$p = 0.04$) are measured when indenting in the transverse plane (i.e. more aligned with the mineralized collagen fibers) with respect to the longitudinal plane. Conversely, an opposing trend (decrease of ∼5%, $p = 0.11$) is detected in the mineral content around the indents between the two planes.

4. Discussion

Combining multiple high-resolution techniques at the same locations, we investigated the mineralized region of two types of fibrocartilage that are contiguous but fulfill different tasks and the underlying subchondral bone. We found that mFC is globally less mineralized and, consequently, less stiff and hard than subchondral bone. Despite these differences, mFC uses mineral reinforcements in a very efficient manner: it needs a smaller fraction of calcium than subchondral bone to reach the same local tissue stiffness and hardness. We uncovered differences between E- and P-mFC in fiber arrangements and in the spatial variation of mechanical properties. We found that local mechanical properties are strikingly uniform across E-mFC (which shows highly aligned fibers) while an additional stiffness gradient, independent from the flat profile of the mineral content, is observed within P-mFC (where fiber organization is very heterogeneous).

Considering mineral content, a similar trend (i.e. mFC less mineralized than bone) was reported at the tendon insertions of the greater trochanter in 6–8 months old rats [40]. At the same location, larger animals (sheep, 3–5 years old) and humans (59–64 years old) seem to have an opposite behavior [40]. Moving to calcified articular cartilage, a higher mineralization level than in bone was measured at human patellae [18] and femoral heads [44]. Conversely, at femoral heads of smaller animals (i.e., 6 months old rabbit) no significant difference was found [19]. In mineralized tissues, the measured degree of mineralization depends on several factors including the extracellular matrix [3,18], the presence of nanochannels [45], the mineralization kinetic (i.e. the speed of increase in mineral content) [41,46], the turnover rate (i.e. the remodeling speed of the tissue) [47] and the modality of ion/precursor transport to the mineralizing sites [48–50]. An explanation of the higher calcium content of calcified cartilage may be the larger extrafibrillar space occupied by water in unmineralized cartilage, which is then replaced by mineral in calcified cartilage [51]. However, this does not clarify our findings. Unlike larger mammals, small animals have a relatively long skeletal maturation: growth in rats is often not completed before 35 weeks of age [52]. At the end of post-natal development, the enthesis is considered as a matured tissue [53]. Yet, during growth, portions of the tendon are replaced by unmineralized cartilage, the latter getting mineralized (as evident from the former tidemarks, **Fig. S6**b) and older calcified cartilage is (at least partially) remodeled into subchondral bone [54]. This may explain the lower degree of mineralization of cartilage found in growing rodents.

Analyzing Ca-Er relationship (**Fig. 3**) allowed two main conclusions. First, using a staggered model for mineral packing in an organic matrix [42] provided a good fit to the mineralization-modulus relation, with both FCs and subchondral bone lying on similar contour lines. This indicates that the aspect ratio of mineral platelets is comparable in both tissues. Second, subchondral bone shows a higher mineral content than mFC to reach a specific stiffness level. This is in contrast with previous results on human (articular) calcified cartilage by Gupta and colleagues [18]. The authors considered the organic matrix (type II collagen in cartilage and type I in bone) as a possible reason for different mechanical properties, perhaps due to changes in the mineral-collagen packing. Recently, more evidence is supporting the active role of the collagen matrix in introducing pre-stresses in mineralized tissue. Such pre-stresses depend on specifics of the collagen matrix and crucially influence the mechanical tissue properties [55,56]. Mineral collagen packing in FC may be different than in articular cartilage owing to a different mixture of collagen type II and III [8,9].

Fiber architecture is a key player for the mechanical efficiency of enthesis. Previous studies have focused on fiber arrangement, particularly when approaching the enthesis from the soft-tissue side [6,9,16,57–60]. Data from Achilles tendon insertions indicate that tendon fibers branch into much thinner interface fibers, spread out and enter FC [9,58]. Within FC, fibers seem to be less aligned than in tendons [61] and ligaments [62]. Characterizations of fiber deformation (considering Achilles tendon and rotator cuff insertions) suggest that different groups of fibers are loaded depending on the angle of remote force application [9,16,63], allowing the enthesis to resist substantial and continuous changes regarding the direction of the tendon force. Several previous works have considered the soft and fibrous side of the enthesis (featuring tendon and uFC) [6,9,58,60]. Here, we complemented current knowledge by following fibers inside mFC and subchondral bone, considering two mutually orthogonal planes. For that purpose, we used sample preparation and measurement techniques which are appropriate for the characterization of mineralized tissues but which are much less useful in characterizing the unmineralized counterparts. A central finding for the interpretation of our result is a very strong SHG signal within enthesis FC (**Fig. 1** and **S7**), likely indicating a high alignment of mineralized collagen fibers. Investigation of the transverse direction confirms fiber anisotropy, with a weak SHG signal as expected when fibers are perpendicular to the imaging plane (**Fig. 6**). Fiber arrangement has a pivotal impact on the local mechanical behavior. Firstly, structural anisotropy is directly reflected into mechanical anisotropy with a higher modulus obtained when indenting along the fibers (transverse plane) than perpendicular to them (sagittal plane). This is further emphasized by the slight decrease in mineral content in the transverse plane, suggesting that the difference in tissue modulus between the two directions cannot be due to variations in mineral content. Mechanical anisotropy is a well-known feature of osteonal and lamellar bone; here we show that even mineralized fibrocartilage at the enthesis is anisotropic, with a similar degree of anisotropy of those tissues [64–66]. Additionally, spatial variations of tissue modulus (and hardness) mirrored very closely the behavior of calcium content: except for a steep gradient across the interface between unmineralized and mineralized tissues, mineral content, elastic modulus and hardness had a remarkably constant profile (**Fig. 5**). At odds with this behavior is the overall increase of elastic modulus inside P-mFC, not accompanied by variations in mineral content (**Fig. 5**). Fiber architecture is probably responsible for this discrepancy: P-mFC has fibers spreading out, branching, intertwining and showing curved paths going around pores (**Fig. 1**). Despite these dissimilarities, the two FCs have a comparable behavior across the transition between unmineralized and mineralized tissues. Using high-resolution (sub-micrometer) qBEI, we observed a steep gradient in mineral content occurring within less than 14 µm (**Fig. 4**), with no differences between enthesis and periosteal regions. Localized compositional gradients are well-known features of enthesis. Depending on anatomical location and measuring techniques, the width of the unmineralized-to-mineralized transition zone ranges from about 10 to 100 µm [10,12,53,67–70]. Experimental and computational works have linked compositional to mechanical gradients [71–74]. Although restricted to an extremely small region, the mechanical modulations should help solve stress and strain incompatibilities between soft and hard tissues [11,75], enhancing failure resistance at the insertion site [16,69]. Assuming that the interfacial material gradient is devoted to reducing stress concentration, the question arises whether the distinct spatial profiles observed in the two mFC may reflect different functional requirements of the two locations. To answer this question, we used a simple 2D model of staggered mineral crystals glued together by an elastoplastic protein matrix (details in Supplementary Material), the "tunability" in stiffness, strength and energy absorption as a function of mineral volume fraction can be estimated (**Fig. S10**). Increasing mineralization of collagen fibers enhances stiffness and strength but decreases energy absorption. Overall, our finding suggests that E-mFC needs to be strong along the prevalent pulling direction of the tendon. To a first approximation, a strong material should have highly aligned fibers and should not include components with low mineral content (and low strength) as they may dominate the overall failure strength (assuming a serial arrangement with the applied load [76]). This may explain the flat profile observed at E-mFC. Such high strength may, however, come at the expenses of toughness. Although we did not perform a fracture study, long parallel cracks likely resulting from sample preparation, were mainly observed inside E-mFC rather than in P-mFC (**Fig. 1**c), further suggesting that the high anisotropy is probably aiming at enhancing tensile strength rather than toughness. P-mFC is a way more heterogeneous material, showing an intricate fiber organization and a gradual increase in tissue modulus. While material heterogeneity may favor damage resistance [77], the elastic modulus gradient should allow to resist compressive loading of the tendon (pressing against the bone during joint rotation) in a progressive manner, to avoid potentially high stresses which may harm both tissues.

Concerning limitations, it should be noted that tissues were tested dehydrated, although we are aware that hydration has a large impact on the local mechanical properties [78,79]. Indenting dehydrated bones typically lead to an overestimation of reduced modulus and hardness [18]. Sample dehydration may also impact collagen packing and organization; this effect should be stronger in tendon and unmineralized FC then in mineralized tissues where water is (at least partially) replaced by mineral. However, to perform a correlative analysis, we had to follow preparation protocols enabling different techniques on the same samples. Being mainly interested in relative differences between mineralized tissues and locations, we would expect dehydration to have a comparable impact on those tissues. Our mechanical analysis was restricted to reduced modulus and hardness. The required lateral spacing between indents imposes a constraint on the spatial resolution of nanoindentation, which is much lower than the sub-micrometer resolution of qBEI and SHG. In principle, a substantial increase in the lateral resolution of the mechanical characterization could be obtained using modulus mapping [80] or with contact resonance force microscopy [19]. Considering SHG, we did not attempt a quantification of the SHG signal as this would require additional assumptions on fiber packing and phase matching [33,81]. Moreover, these quantities cannot be easily decoupled from fiber orientation. One additional challenge is the presence of a complex hierarchical porosity, hampering the definition of representative subregions with constant dimensions. In view of the striking differences of fiber arrangement between enthesis and periosteal regions, we judged that a qualitative analysis of SHG images was sufficient for our investigation. Finally, it should be considered that our sample size was limited due to the time-consuming analysis performed. Indeed, our research strategy, common to many studies focusing on micro- and nanoscopic material properties [3,18,19,45,82], was to perform a thorough characterization of a limited number of samples, rather than testing more samples to a lesser extent. Despite the shortcomings of this choice, all measured compositional, structural and mechanical quantities were consistent in all samples and locations analyzed. In a previous work, we characterized the microstructure of bone and mFC with micro-CT considering a larger number of animals (*n* = 7) and of the same strain and age. All samples had a striking similar microstructural porosity suggesting a reduced biological variability of the chosen animal model and anatomical location. Limiting the number of animals (compatible with the study aims) is also in line with the global effort to reduce animal usage in experimental research. The present multimodal approach can be used to investigate medically relevant scenarios, considering for example the impact on mFC of over or unloading [83], inflammation mimicking enthesopathies, or aging. These studies comparing different groups would need a larger number of samples, which can be calculated based on power analysis and effect size.

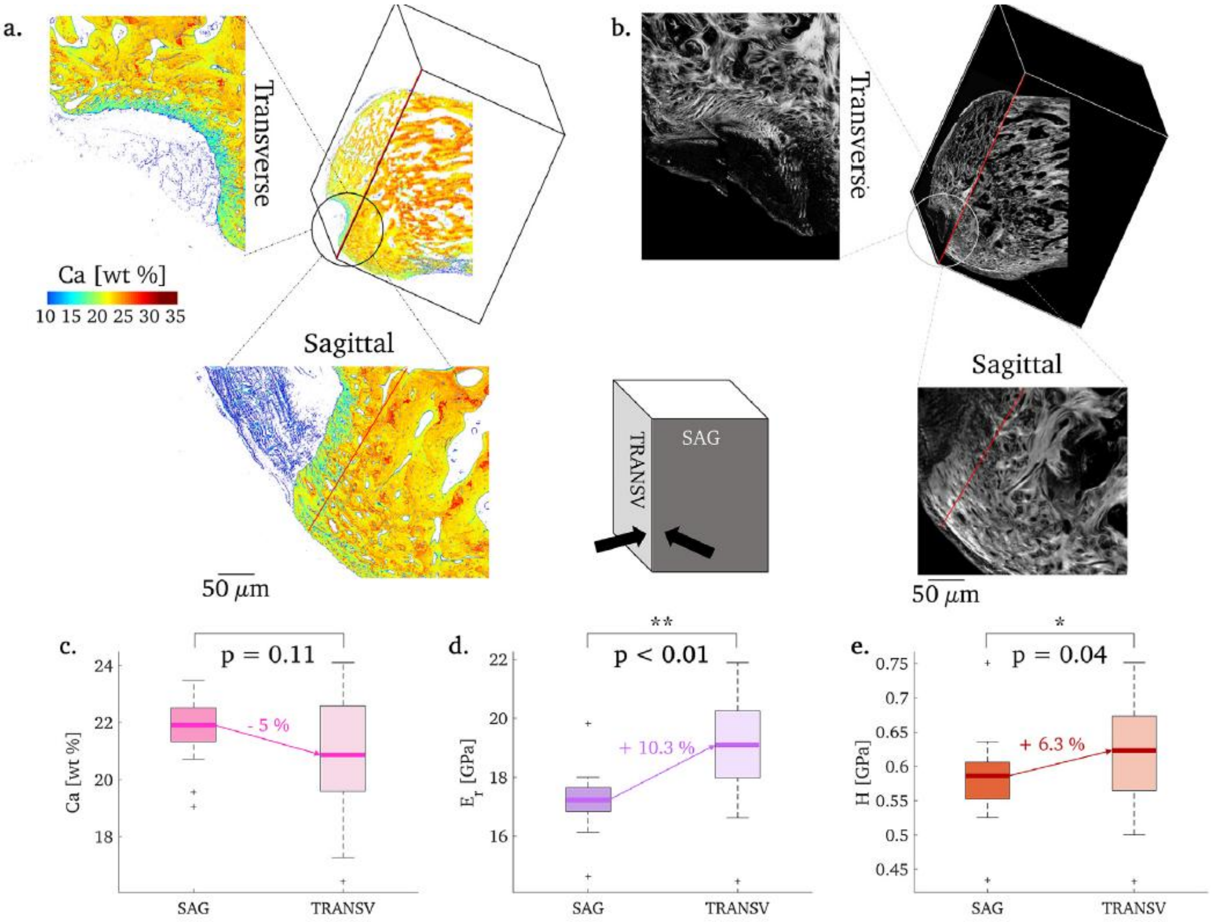

Fig. 6. Mineralization, fiber organization and material properties measured on E-mFC considering two mutually orthogonal planes. Sagittal and transverse (a) qBEI maps and (b) SHG images. Box plots showing (c) calcium content (Ca), (d) reduced modulus (E_r) and (e) hardness (H) for a set of indentation points (*n* = 21) selected on adjacent locations within E-mFC on both planes. Boxes range from the 25th to the 75th percentiles. Points positioned more than one interquartile length away from the boxes were considered outliers and plotted individually (+). Whiskers extend to the most extreme data point which is not an outlier. Thick lines represent the mean value. ∗∗ $P < 0.01$, ∗ $P < 0.05$.

5. Conclusions

The combination of nanoindentation, qBEI and SHG imaging provided powerful insights into the structure and functioning of FC. We highlighted that E-mFC and P-mFC are mechanically efficient tissues attaining their stiffness and hardness by using less mineral than bone would require. The two FCs had different fibers organization and spatial modulation of mechanical properties. Spatially constant tissue modulus and hardness, combined with highly aligned collagen fibers were observed at enthesis FC, mirroring the previously detected microstructural anisotropy. We hypothesize that such construction strategy enhances strength at the tendon insertion. Our work demonstrates the adaptability, versatility and efficiency of FC in helping bone to cope with challenging mechanical tasks.

Declaration of Competing Interest

The authors declare that they have no known competing financial interests or personal relationships that could have appeared to influence the work reported in this paper.

Acknowledgements

AT is a FRIA (Fund for Research Training in Industry and Agriculture) grant holder (n°5129219F). We warmly thank Luc Duwez from University of Liege, GIGA, for his essential help with sample extraction. We wish to thank Petra Keplinger, Sonja Lueger and Phaedra Messmer from LBIO for the excellent sample preparation. MH and SB are grateful for financial support from the AUVA (Research funds of the Austrian workers' compensation board) and OEGK (Austrian Social Health Insurance Fund). MR and RW acknowledge support from the Max Planck Queensland centre for the Materials Science of Extracellular Matrices.

Published in : Acta Biomaterialia (2023), vol. 166, pp. 409–418
DOI: 10.1016/j.actbio.2023.04.018
Status : Postprint (Author's version)

Supplementary materials

SUPPLEMENTARY FIGURES

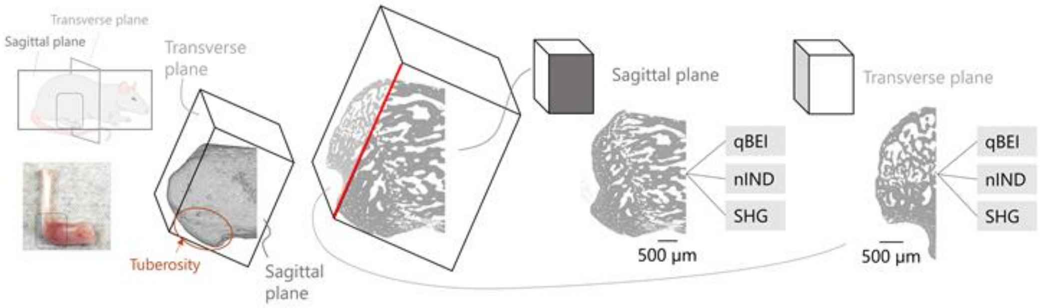

Figure S1. Schematic of the sagittal and transverse planes on a representative sample, and corresponding investigation techniques: qBEI (quantitative backscattered electron imaging), nIND (nanoindentation), SHG (second harmonic generation). The picture of the tendon-bone construct was taken during a typical sample extraction procedure.

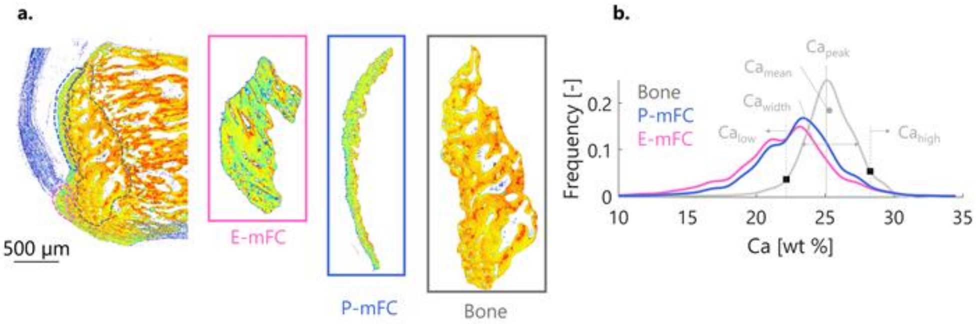

Figure S2. (a) qBEI maps and regions of interest used to measure the mineral content of the entire enthesis mineralized fibrocartilage (E-mFC), periosteal mFC (P-mFC) and subchondral bone regions, on a representative sample. (b) Frequency distributions of calcium content, obtained by pooling together data from both samples.

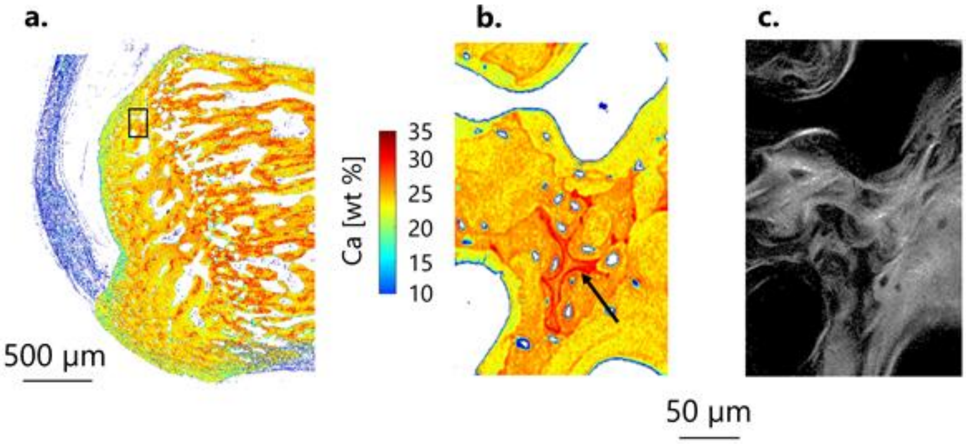

Figure S3. Illustration of a cartilaginous inclusion in bone probably formed during endochondral ossification and not removed by remodeling [1,2]. The high mineral content is clearly visible in qBEI as indicated with a black arrow (a) and it is reflected into a blurry SHG signal (b), likely indicating less ordered endochondral bone.

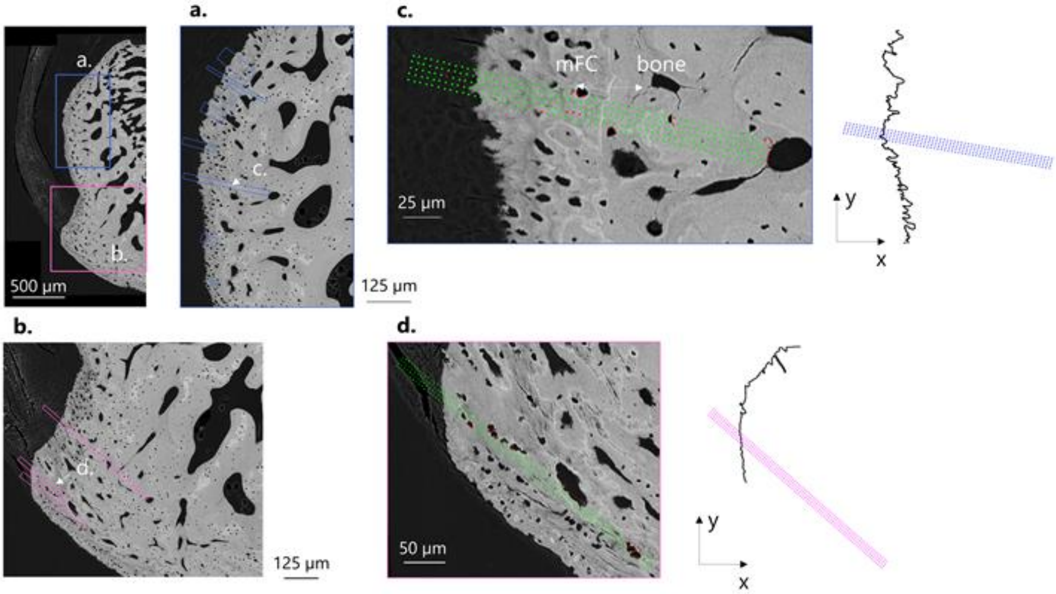

Figure S4. Overview of several nanoindentation grids on a representative sample at the periosteal (a) and enthesis (b) region. Close-up on typical scanning grids at the periosteal (c) and enthesis (d) region, showing the rejected indents in red and the accepted ones in green, as well as the resulting contour extraction of the interface between unmineralized fibrocartilage (uFC) and mFC for distance-to-surface measurement.

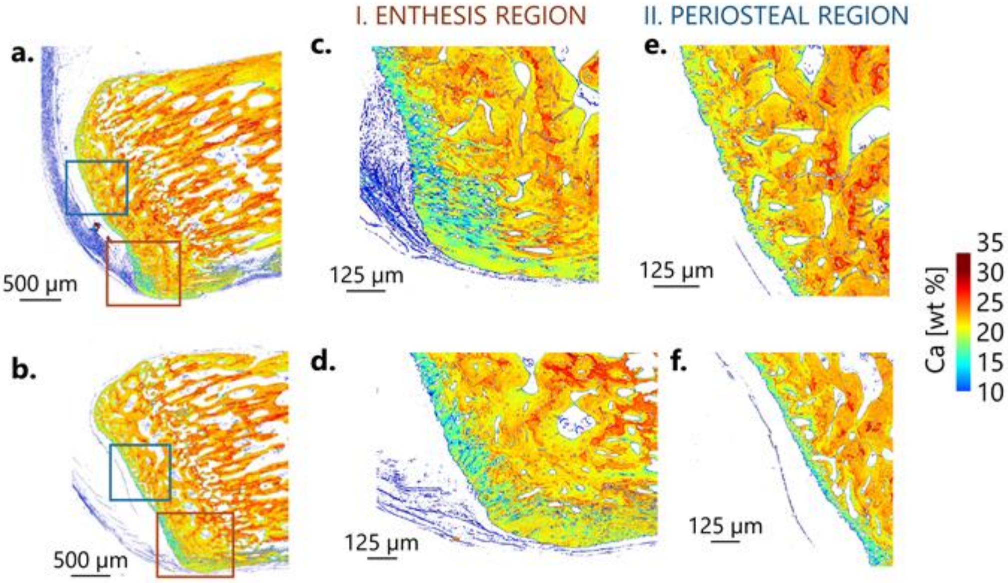

Figure S5. Full qBEI overviews (a and b) and close-up on the regions of interest including enthesis and periosteal locations for the measured samples not shown in the main manuscript. As in one sample (bottom row) the tuberosity could not be clearly spotted and, consequently, both mFC layers were very thin, the sample was not considered for further quantitative analysis.

Published in : Acta Biomaterialia (2023), vol. 166, pp. 409–418
DOI: 10.1016/j.actbio.2023.04.018
Status : Postprint (Author's version)

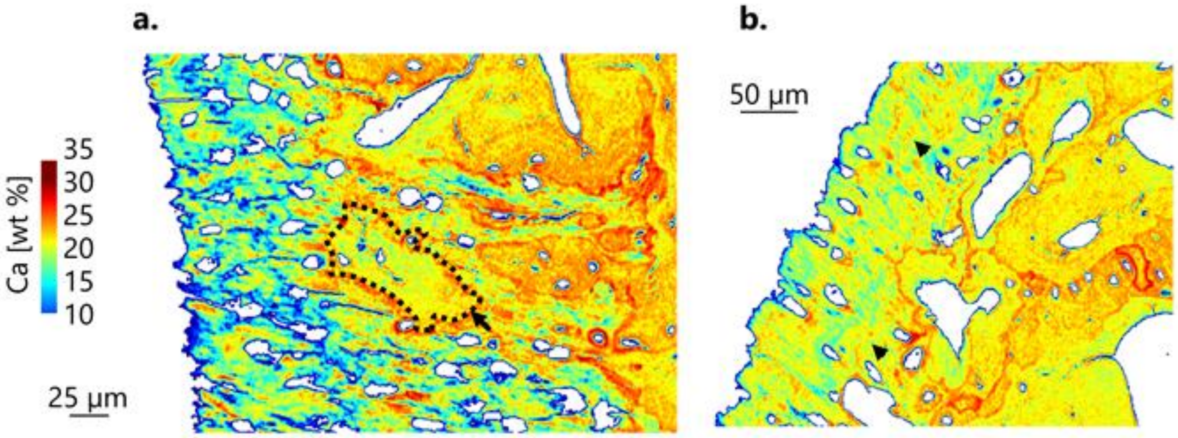

Figure S6. Characteristic features on qBEI images. (a) Bone island (contoured in black, and indicated by the black arrow) within periosteal FC. (b) Former tidemarks (black arrows) within periosteal FC.

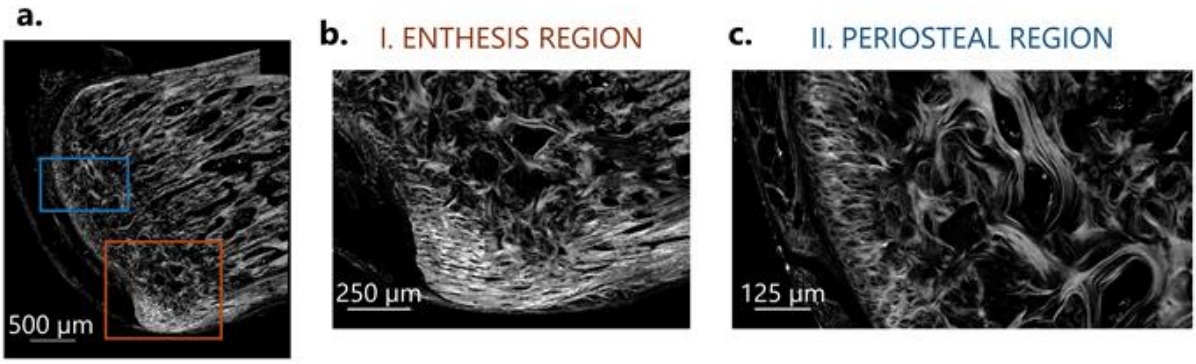

Figure S7. Full SHG overview (a), and inset into the (b) enthesis and (c) periosteal areas, for the second sample not shown in the main manuscript.

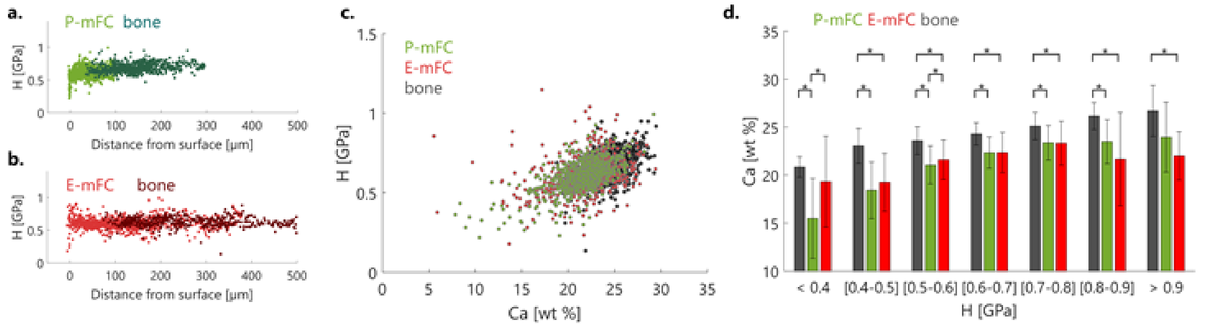

Figure S8. (a, b) Spatial evolution of hardness (H) at (a) periosteal and (b) enthesis region for all measured points. (c) Hardness as a function of local calcium weight percentage in mFC and bone at periosteal and enthesis region. (d) Averaged calcium content values for mineralized cartilage and bone needed to obtain hardness ranging from 0.4 to 0.9 GPa (bin width 0.1 GPa) * $P < 0.05$.

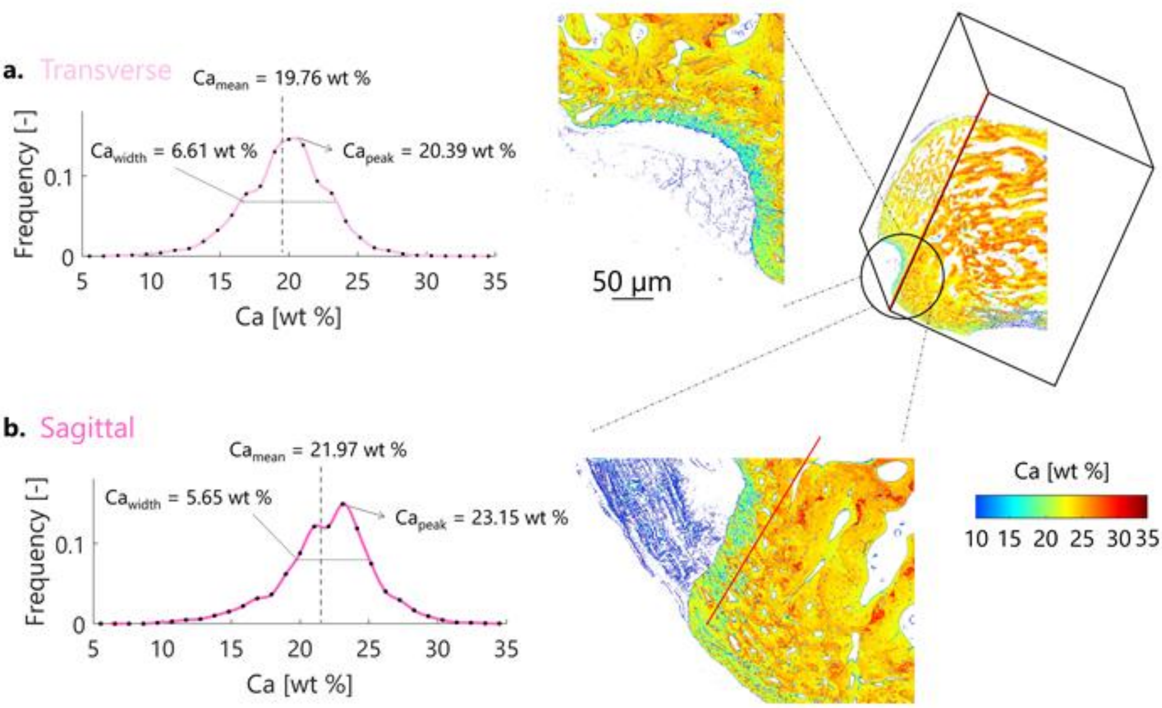

Figure S9. Frequency distributions of calcium content for transverse (a) and sagittal (b) enthesis mFC measured based on the entire tissue region, and represented using a smoothing spline.

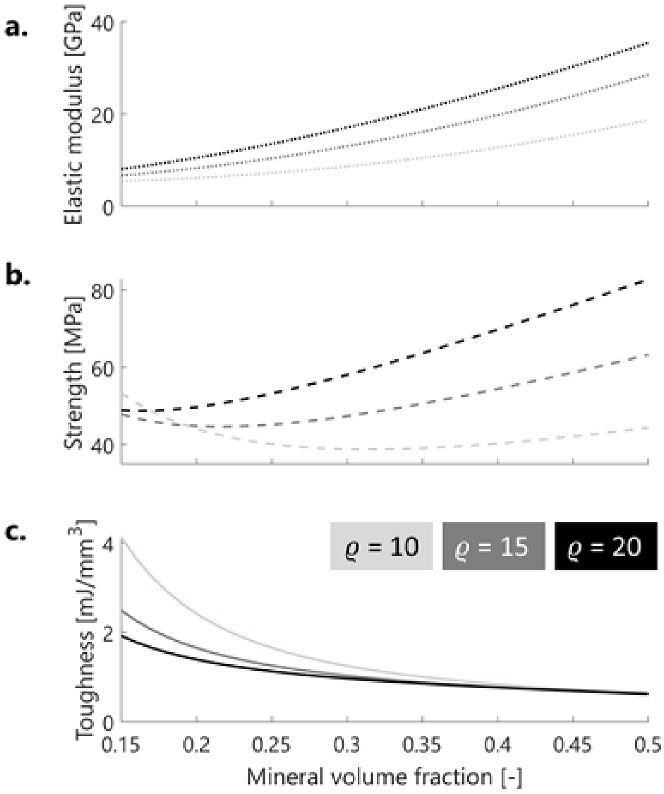

Figure S10. Modulation of (a) elastic modulus, (b) strength and (c) toughness as a function of the mineral volume fraction and for several mineral aspect ratios ϱ, as estimated by a staggered composite model.

Assuming a staggered composite model with elastic-brittle mineral crystals glued together by a ductile elasto-plastic protein matrix, the elastic modulus E_C as a function of the mineral volume fraction φ is given by [42]:

$$E_C = \phi\,\frac{E_M}{\kappa} + (1 - \phi)E_p \tag{1}$$

$$\kappa = 1 + \frac{1-\phi}{\phi}\,\frac{4}{\varrho^2}\,\frac{E_M}{G_P} \tag{2}$$

With the Young's modulus of hydroxyapatite E_m = 100 GPa, the shear modulus of the organic protein matrix $G_p = \gamma\, E_p$, where $\gamma \approx 0.4$, and the Young's modulus of the organic protein matrix E_p = 5 GPa. It should be noted that the modulus of the hydrated proteinaceous collagen matrix should be around 1-2 GPa. The value used here, which is based on the (few) indentations points placed into unmineralized fibrocartilage, is representative for a PMMA–collagen composite as the tissues were dehydrated and then infiltrated by PMMA. The mineral platelets aspect ratio ϱ was allowed to vary from 10 to 20.

To connect calcium content with mineral volume fraction, one can use the following relationships [82]:

$$\phi = \frac{HA}{HA + (1\text{-}HA)\left(\frac{\rho_{HA}}{\rho_{org}}\right)} \tag{3}$$

$$HA = 2.5066\ Ca_{mean} \tag{4}$$

With hydroxyapatite density ρ_{HA} = 3.18 g cm^{-3} and organic matrix density ρ_{org} = 1.47 g cm^{-3}.

The model further assumes that beyond a critical shear stress τ_p^* the matrix flows plastically. In in the staggered arrangement the stress on the mineral particles σ_m and the shear stress inside the protein matrix τ_p are linked by:

$$\tau_p = \frac{2}{\varrho}\sigma_m \tag{5}$$

Therefore, if τ_p^* is smaller than the fracture stress of the brittle mineral σ_m^f (according to Eq. 5), the matrix will flow before the mineral crystals can break. Here, we assumed σ_m^f=100 MPa and $\tau_p^* = G_p\eta_p^y$ with η_p^y=0.8% being the critical yield shear strain at which the protein matrix starts plastic flow (likely due to breaking of ionic bonds [82]). Strength is measured as the maximum stress reached by the staggered protein-mineral composite at the end of the elastic region right before plastic flow, according to:

$$\sigma_C^{max} = E_c\varepsilon_C = E_c\varepsilon_m = E_c\frac{k\rho}{2E_m}\tau_p^* \tag{6}$$

Toughness is estimated at the area under the overall stress-strain curve of the composite. Once the matrix starts to flow, the stress in the staggered composite does not increase but the strain does, till the matrix reaches its fracture shear strain $\eta_p^f = 8\%$. The maximum strain on the composite at the end of the plastic flow of the protein matrix is given by:

$$\varepsilon_C^{max} = \varepsilon_m + \frac{2}{\varrho}\frac{1-\phi}{\phi}\eta_p^f = \frac{k\rho}{2E_m}\tau_p^* + \frac{2}{\varrho}\frac{1-\phi}{\phi}\eta_p^f \tag{7}$$

SUPPLEMENTARY TABLES

Table S1

Global properties of bone compared with the two mFC types (periosteal and insertional), for both samples pooled together (data for each separate sample provided within the brackets).

Parameter	Bone *(Region I)*	*Δ (I-II)*	Periosteal mFC *(Region II)*	*Δ (II-III)*	Insertional mFC *(Region III)*	*Δ (I-III)*
Mineralization properties (based on 4 x 4 pixel average around the indent location)						
Ca_{mean} [wt %]	24.41 [24.73 24.26]	*-11.63%*	21.57 [22.06 21.49]	*+1.3%*	21.85 [21.03 22.41]	*-10.49%*
Ca_{peak} [wt %]	24.36 [24.47 24.27]	*-9.24%*	22.11 [22.2 22.06]	*-0.9%*	21.91 [21.71 22.29]	*-10.06%*
Ca_{width} [wt %]	2.53 [2.62 2.5]	*+28.46%*	3.25 [2.56 3.48]	*-6.15%*	3.05 [2.56 3.48]	*+20.55%*
Ca_{low} [%]	5	*+929%*	51.45 [40.26 53.48]	*-1.9%*	50.47 [66.76 39.21]	*+909.4%*
Ca_{high} [%]	5	*-91.6%*	0.42 [1.17 0.43]	*+319.05%*	1.76 [1.7 1.8]	*-64.8%*
Mechanical properties						
$E_{r,\,mean}$ [GPa]	21.13 [22.05 20.31]	*-18.88%*	17.14 [17.61 17.06]	*-1.52%*	16.88 [16.53 17.09]	*-20.11%*
$E_{r,\,peak}$ [GPa]	21.49 [21.59 19.53]	*-19.08%*	17.39 [17.03 17.58]	*-0.86%*	17.24 [16.17 16.96]	*-19.78%*
$E_{r,\,width}$ [GPa]	5.22 [4.27 4.7]	*-25.48%*	3.86 [4.22 3.81]	*-31.61%*	2.64 [2.76 2.66]	*-49.42%*
$E_{r,\,low}$ [%]	5	*+947%*	52.35 [47.75 53.13]	*+27.98%*	67 [71.3 63.63]	*+1240%*
$E_{r,\,high}$ [%]	5	*-96.8%*	0.16 [0.2 0.32]	*-100%*	0	*-100%*
Hardness properties						
H_{mean} [GPa]	0.66 [0.68 0.64]	*-7.58%*	0.61 [0.59 0.61]	*-1.64%*	0.6 [0.59 0.62]	*-9.09%*
H_{peak} [GPa]	0.65 [0.67 0.61]	*-4.61%*	0.62 [0.6 0.63]	*-4.84%*	0.59 [0.58 0.59]	*-9.23%*
H_{width} [GPa]	0.17 [0.16 0.17]	*+5.88%*	0.18 [0.13 0.18]	*-22.22%*	0.14 [0.13 0.14]	*-17.65%*
H_{low} [%]	5	*+346.8%*	22.34 [26.69 21.49]	*+3.45%*	23.11 [25.84 20.04]	*+362.2%*
H_{high} [%]	5	*-55.4%*	2.23 [1.43 2.54]	*+80.27%*	4.02 [1.82 5.78]	*-19.6%*

Table S2

Mineralization properties of bone compared with the periosteal and insertional mFC type (based on entire tissue region), for both samples pooled together (data for each separate sample provided within the brackets).

Parameter	Bone *(Region I)*	*Δ (I-II)*	Periosteal mFC *(Region II)*	*Δ (II-III)*	Insertional mFC *(Region III)*	*Δ (I-III)*
Ca$_{mean}$ [wt %]	25.26 [25.5 25.12]	*-9.2%*	22.94 [23.27 22.68]	*-4.2%*	21.97 [21.5 22.45]	-13%
Ca$_{peak}$ [wt %]	25.15 [25.26 25.12]	*-6.9%*	23.41 [23.58 23.32]	*-1.1%*	23.15 [23.03 23.29]	-7.9%
Ca$_{width}$ [wt %]	3.68 [4.06 3.39]	*+44.3%*	5.31 [5.39 5.22]	*+6.4%*	5.65 [6 5.31]	+53.5%
Ca$_{low}$ [%]	5	*+622.4%*	36.12 [31.93 39.38]	*+35.5%*	48.93 [55.24 42.39]	+878.6%
Ca$_{high}$ [%]	5	*-42.8%*	2.86 [3.91 2.04]	*-11.5%*	2.53 [2.15 2.92]	-49.4%

Table S3

Parameters of the exponential function fitting the relationship between calcium content and mechanical properties ($Ca=a\ e^{b\ E_r}$ or $Ca=a\ e^{b\ H}$) for both samples pooled together, and corresponding t-values.

Parameter	Ca-E$_r$ in E-mFC	Ca-H in E-mFC	Ca-E$_r$ in P-mFC	Ca-H in P-mFC	Ca-E$_r$ in bone	Ca-H in bone
a [wt %]	10.68	0.38	6.42	0.25	10.69	0.27
t-value for a [-]	32.94	20.66	21.98	21.34	19.26	18.88
b [GPa^{-1}]	0.02	0.02	0.04	0.04	0.03	0.04
t-value for b [-]	15.3	9.8	22.04	19.12	13.18	16.7

Table S4

Parameters of the sigmoid function fitting the non-mineralized to mineralized tissue transition

$Ca\ (dist) = Ca_0 + \frac{\alpha}{1+e^{-\beta(dist-dist0)}}$ and $TW = dist(\ Ca = 0.995*\alpha + Ca_0\ ) - dist(\ Ca = 0.005*\alpha + Ca_0\ )$ for both samples pooled together.

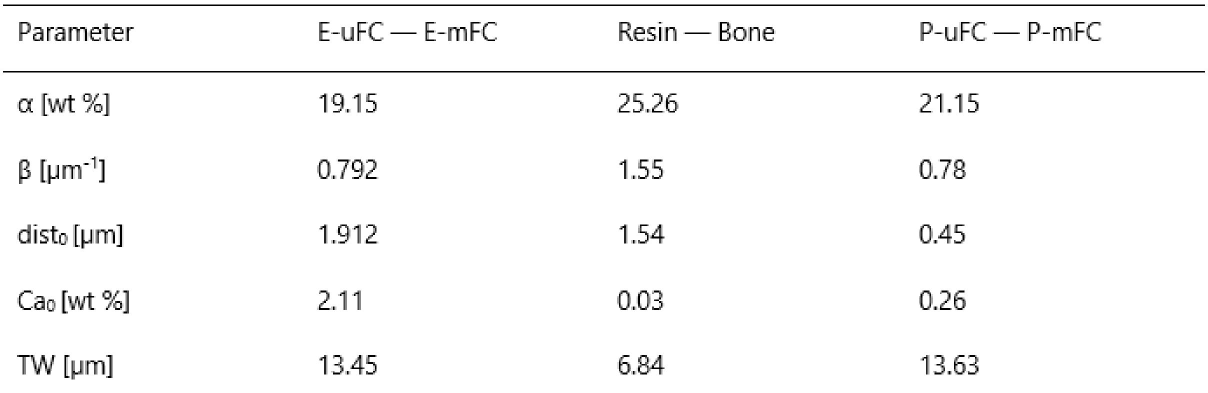

Parameter	E-uFC — E-mFC	Resin — Bone	P-uFC — P-mFC
α [wt %]	19.15	25.26	21.15
β [µm^{-1}]	0.792	1.55	0.78
dist$_0$ [µm]	1.912	1.54	0.45
Ca$_0$ [wt %]	2.11	0.03	0.26
TW [µm]	13.45	6.84	13.63

REFERENCES

[1] F.L. Bach-Gansmo, S.C. Irvine, A. Brüel, J.S. Thomsen, H. Birkedal, Calcified cartilage islands in rat cortical bone, Calcified Tissue International. 92 (2013) 330–338.

[2] A. Shipov, P. Zaslansky, H. Riesemeier, G. Segev, A. Atkins, R. Shahar, Unremodeled endochondral bone is a major architectural component of the cortical bone of the rat (Rattus norvegicus), Journal of Structural Biology. 183 (2013) 132–140.

[3] H.S. Gupta, S. Schratter, W. Tesch, P. Roschger, A. Berzlanovich, T. Schoeberl, K. Klaushofer, P. Fratzl, Two different correlations between nanoindentation modulus and mineral content in the bone–cartilage interface, Journal of Structural Biology. 149 (2005) 138–148.

[4] I. Jäger, P. Fratzl, Mineralized collagen fibrils: a mechanical model with a staggered arrangement of mineral particles, Biophysical Journal. 79 (2000) 1737–1746.

[5] P. Fratzl, R. Weinkamer, Nature's hierarchical materials, Progress in Materials Science. 52 (2007) 1263–1334.

References

[1] V.C. Mow, W.Y. Gu, F.H. Chen, Structure and function of articular cartilage, Basic Orthop. Biomech. Mechano-Biol. 3 (2005) 181–258.

[2] L. Han, A.J. Grodzinsky, C. Ortiz, Nanomechanics of the cartilage extracellular matrix, Annu. Rev. Mater. Res. 41 (2011) 133–168.

[3] I. Zizak, P. Roschger, O. Paris, B.M. Misof, A. Berzlanovich, S. Bernstorff, H. Amenitsch, K. Klaushofer, P. Fratzl, Characteristics of mineral particles in the human bone/cartilage interface, J. Struct. Biol. 141 (2003) 208–217.

[4] M. Benjamin, J.R. Ralphs, Fibrocartilage in tendons and ligaments—an adaptation to compressive load, J. Anat. 193 (1998) 481–494.

[5] A.C. Abraham, T.L.H. Donahue, From meniscus to bone: a quantitative evaluation of structure and function of the human meniscal attachments, Acta Biomater. 9 (2013) 6322–6329.

[6] A.J. Boys, J.A. Kunitake, C.R. Henak, I. Cohen, L.A. Estroff, L.J. Bonassar, Understanding the stiff-to-compliant transition of the meniscal attachments by spatial correlation of composition, structure, and mechanics, ACS Appl. Mater. Interfaces 11 (2019) 26559–26570.

[7] K.N. Hauch, M.L. Oyen, G.M. Odegard, T.H. Donahue, Nanoindentation of the insertional zones of human meniscal attachments into underlying bone, J. Mech. Behav. Biomed. Mater. 2 (2009) 339–347.

[8] A.D. Waggett, J.R. Ralphs, A.P. Kwan, D. Woodnutt, M. Benjamin, Characterization of collagens and proteoglycans at the insertion of the human Achilles tendon, Matrix Biol. 16 (1998) 457–470.

[9] L. Rossetti, L.A. Kuntz, E. Kunold, J. Schock, K.W. Müller, H. Grabmayr, J. Stolberg-Stolberg, F. Pfeiffer, S.A. Sieber, R. Burgkart, The microstructure and micromechanics of the tendon–bone insertion, Nat. Mater. 16 (2017) 664–670.

[10] J.P. Spalazzi, A.L. Boskey, N. Pleshko, H.H. Lu, Quantitative mapping of matrix content and distribution across the ligament-to-bone insertion, PLoS One 8 (2013) e74349.

[11] A.Y. Uzan, O. Milo, Y. Politi, B. Bar-On, Principles of elastic bridging in biological materials, Acta Biomater. (2022).

[12] A. Tits, D. Ruffoni, Joining soft tissues to bone: insights from modeling and simulations, Bone Rep 14 (2021) 100742.

[13] H.H. Lu, S. Thomopoulos, Functional attachment of soft tissues to bone: development, healing, and tissue engineering, Annu. Rev. Biomed. Eng. 15 (2013) 201.

[14] S. Thomopoulos, G.R. Williams, L.J. Soslowsky, Tendon to bone healing: differences in biomechanical, structural, and compositional properties due to a range of activity levels, J. Biomech. Eng. 125 (2003) 106–113.

[15] S. Thomopoulos, G.R. Williams, J.A. Gimbel, M. Favata, L.J. Soslowsky, Variation of biomechanical, structural, and compositional properties along the tendon to bone insertion site, J. Orthop. Res. 21 (2003) 413–419.

[16] M. Golman, A.C. Abraham, I. Kurtaliaj, B.P. Marshall, Y.J. Hu, A.G. Schwartz, X.E. Guo, V. Birman, P.J. Thurner, G.M. Genin, Toughening mechanisms for the attachment of architectured materials: the mechanics of the tendon enthesis, Sci. Adv. 7 (2021) eabi5584.

[17] C. Camy, T. Brioche, K. Senni, A. Bertaud, C. Genovesio, E. Lamy, T. Fovet, A. Chopard, M. Pithioux, S. Roffino, Effects of hindlimb unloading and subsequent reloading on the structure and mechanical properties of Achilles tendon-to-bone attachment, FASEB J. 36 (2022).

[18] H.S. Gupta, S. Schratter, W. Tesch, P. Roschger, A. Berzlanovich, T. Schoeberl, K. Klaushofer, P. Fratzl, Two different correlations between nanoindentation modulus and mineral content in the bone–cartilage interface, J. Struct. Biol. 149 (2005) 138–148.

[19] S.E. Campbell, V.L. Ferguson, D.C. Hurley, Nanomechanical mapping of the osteochondral interface with contact resonance force microscopy and nanoindentation, Acta Biomater. 8 (2012) 4389–4396.

[20] K. Madi, K.A. Staines, B.K. Bay, B. Javaheri, H. Geng, A.J. Bodey, S. Cartmell, A.A. Pitsillides, P.D. Lee, In situ characterization of nanoscale strains in loaded whole joints via synchrotron X-ray tomography, Nat. Biomed. Eng. 4 (2020) 343–354.

[21] M. Benjamin, D. McGonagle, The anatomical basis for disease localisation in seronegative spondyloarthropathy at entheses and related sites, J. Anat. 199 (2001) 503–526.

[22] A.S. Kehl, M. Corr, M.H. Weisman, Enthesitis: new insights into pathogenesis, diagnostic modalities, and treatment, Arthritis & Rheumatology (Hoboken, NJ) 68 (2016) 312.

[23] J.-F. Kaux, P.V. Drion, A. Colige, F. Pascon, V. Libertiaux, A. Hoffmann, L. Janssen, A. Heyers, B.V. Nusgens, C.Le Goff, Effects of platelet-rich plasma (PRP) on the healing of Achilles tendons of rats, Wound Repair Regen. 20 (2012) 748–756.

[24] J.-F. Kaux, P. Drion, V. Libertiaux, A. Colige, A. Hoffmann, B. Nusgens, B. Besançon, B. Forthomme, C.Le Goff, R. Franzen, Eccentric training improves tendon biomechanical properties: a rat model, J. Orthop. Res. 31 (2013) 119–124.

[25] A. Tits, E. Plougonven, S. Blouin, M.A. Hartmann, J.-F. Kaux, P. Drion, J. Fernandez, G.H. van Lenthe, D. Ruffoni, Local anisotropy in mineralized fibrocartilage and subchondral bone beneath the tendon-bone interface, Sci. Rep. 11 (2021) 1–17.

[26] P. Roschger, P. Fratzl, J. Eschberger, K. Klaushofer, Validation of quantitative backscattered electron imaging for the measurement of mineral density distribution in human bone biopsies, Bone 23 (1998) 319–326.

[27] M.A. Hartmann, S. Blouin, B.M. Misof, N. Fratzl-Zelman, P. Roschger, A. Berzlanovich, G.M. Gruber, P.C. Brugger, J. Zwerina, P. Fratzl, Quantitative Backscattered Electron Imaging of bone using a thermionic or a field emission electron source, Calcif. Tissue Int. 109 (2021) 190–202.

[28] P. Roschger, E.P. Paschalis, P. Fratzl, K. Klaushofer, Bone mineralization density distribution in health and disease, Bone 42 (2008) 456–466.

[29] A. Shipov, P. Zaslansky, H. Riesemeier, G. Segev, A. Atkins, R. Shahar, Unremodeled endochondral bone is a major architectural component of the cortical bone of the rat (Rattus norvegicus), J. Struct. Biol. 183 (2013) 132–140.

[30] F.L. Bach-Gansmo, S.C. Irvine, A. Brüel, J.S. Thomsen, H. Birkedal, Calcified cartilage islands in rat cortical bone, Calcif. Tissue Int. 92 (2013) 330–338.

[31] S. Roth, I. Freund, Second harmonic generation in collagen, J. Chem. Phys. 70 (1979) 1637–1643.

[32] R.M. Williams, W.R. Zipfel, W.W. Webb, Interpreting second-harmonic generation images of collagen I fibrils, Biophys. J. 88 (2005) 1377–1386.

[33] X. Chen, O. Nadiarynkh, S. Plotnikov, P.J. Campagnola, Second harmonic generation microscopy for quantitative analysis of collagen fibrillar structure, Nat. Protoc. 7 (2012) 654–669.

[34] M.-A. Houle, C.-A. Couture, S. Bancelin, J. Van der Kolk, E. Auger, C. Brown, K. Popov, L. Ramunno, F. Légaré, Analysis of forward and backward Second Harmonic Generation images to probe the nanoscale structure of collagen within bone and cartilage, J. Biophotonics 8 (2015) 993–1001.

[35] T. Tang, V. Ebacher, P. Cripton, P. Guy, H. McKay, R. Wang, Shear deformation and fracture of human cortical bone, Bone 71 (2015) 25–35.

[36] E. Donnelly, S.P. Baker, A.L. Boskey, M.C. van der Meulen, Effects of surface roughness and maximum load on the mechanical properties of cancellous bone measured by nanoindentation, J. Biomed. Mater. Res. Part A 77 (2006) 426–435.

[37] M.S. Bobji, S.K. Biswas, Estimation of hardness by nanoindentation of rough surfaces, J. Mater. Res. 13 (1998) 3227–3233.

[38] W.C. Oliver, G.M. Pharr, An improved technique for determining hardness andelastic modulus using load and displacement sensing indentation experiments, J. Mater. Res. 7 (1992) 1564–1583.

[39] J. Burkey, LOWESS, Locally Weighted Scatterplot Smoothing for linear and non-linear data (enhanced), MATLAB Central File Exchange (2020).

[40] J.E. Shea, R.K. Hallows, R.D. Bloebaum, in: Experimental Confirmation of the Sheep Model For Studying the Role of Calcified Fibrocartilage in Hip Fractures and Tendon Attachments, 266, The Anatomical Record: An Official Publication of the American Association of Anatomists, 2002, pp. 177–183.

[41] D. Ruffoni, P. Fratzl, P. Roschger, K. Klaushofer, R. Weinkamer, The bone mineralization density distribution as a fingerprint of the mineralization process, Bone 40 (2007) 1308–1319.

[42] I. Jäger, P. Fratzl, Mineralized collagen fibrils: a mechanical model with a staggered arrangement of mineral particles, Biophys. J. 79 (2000) 1737–1746.

[43] R. Seidel, A. Roschger, L. Li, J.J. Bizzarro, Q. Zhang, J. Yin, T. Yang, J.C. Weaver, P. Fratzl, P. Roschger, Mechanical properties of stingray tesserae: high-resolution correlative analysis of mineral density and indentation moduli in tessellated cartilage, Acta Biomater. 96 (2019) 421–435.

[44] V.L. Ferguson, A.J. Bushby, A. Boyde, Nanomechanical properties and mineral concentration in articular calcified cartilage and subchondral bone, J. Anat. 203 (2003) 191–202.

[45] T. Tang, W. Landis, S. Blouin, L. Bertinetti, M.A. Hartmann, A. Berzlanovich, R. Weinkamer, W. Wagermaier, P. Fratzl, Sub-canalicular nanochannel volume is inversely correlated with calcium content in human cortical bone, J. Bone Miner. Res. (2022).

[46] C. Lukas, D. Ruffoni, F.M. Lambers, F.A. Schulte, G. Kuhn, P. Kollmanns-berger, R. Weinkamer, R. Müller, Mineralization kinetics in murine trabecular bone quantified by time-lapsed in vivo micro-computed tomography, Bone 56 (2013) 55–60.

[47] D. Ruffoni, P. Fratzl, P. Roschger, R. Phipps, K. Klaushofer, R. Weinkamer, Effect of temporal changes in bone turnover on the bone mineralization density distribution: a computer simulation study, J. Bone Miner. Res. 23 (2008) 1905–1914.

[48] A. Roschger, P. Roschger, W. Wagermaier, J. Chen, A.F. Van Tol, F. Repp, S. Blouin, A. Berzlanovich, G.M. Gruber, K. Klaushofer, The contribution of the pericanalicular matrix to mineral content in human osteonal bone, Bone 123 (2019) 76–85.

[49] A. Roschger, W. Wagermaier, S. Gamsjaeger, N. Hassler, I. Schmidt, S. Blouin, A. Berzlanovich, G.M. Gruber, R. Weinkamer, P. Roschger, Newly formed and remodeled human bone exhibits differences in the mineralization process, Acta Biomater. 104 (2020) 221–230.

[50] M. Ayoubi, A.F. van Tol, R. Weinkamer, P. Roschger, P.C. Brugger, A. Berzlanovich, L. Bertinetti, A. Roschger, P. Fratzl, 3D interrelationship between osteocyte network and forming mineral during human bone remodeling, Adv. Healthc. Mater. 10 (2021) 2100113.
[51] W. Zhu, J.C. Iatridis, V. Hlibczuk, A. Ratcliffe, V.C. Mow, Determination of collagen-proteoglycan interactions in vitro, J. Biomech. 29 (1996) 773–783.
[52] T. Taguchi, M.J. Lopez, An overview of de novo bone generation in animal models, J. Orthop. Res. 39 (2021) 7–21.
[53] A.G. Schwartz, J.D. Pasteris, G.M. Genin, T.L. Daulton, S. Thomopoulos, Mineral distributions at the developing tendon enthesis, PLoS One (7) (2012) e48630.
[54] M.H. Badi, Calcification and ossification of fibrocartilage in the attachment of the patellar ligament in the rat, J. Anat. 112 (1972) 415.
[55] H. Ping, W. Wagermaier, N. Horbelt, E. Scoppola, C. Li, P. Werner, Z. Fu, P. Fratzl, Mineralization generates megapascal contractile stresses in collagen fibrils, Science 376 (2022) 188–192.
[56] A. Masic, L. Bertinetti, R. Schuetz, S.-W. Chang, T.H. Metzger, M.J. Buehler, P. Fratzl, Osmotic pressure induced tensile forces in tendon collagen, Nat. Commun. 6 (2015) 1–8.
[57] J.L. Sevick, Z. Abusara, S.H. Andrews, M. Xu, S. Khurshid, J. Chatha, D.A. Hart, N.G. Shrive, Fibril deformation under load of the rabbit Achilles tendon and medial collateral ligament femoral entheses, J. Orthop. Res. 36 (2018) 2506–2515.
[58] J. Sartori, H. Stark, Tracking tendon fibers to their insertion–a 3D analysis of the Achilles tendon enthesis in mice, Acta Biomater. 120 (2021) 146–155.
[59] J. Sartori, S. Köhring, S. Bruns, J. Moosmann, J.U. Hammel, Gaining insight into the deformation of achilles tendon entheses in mice, Adv. Eng. Mater. 23 (2021) 2100085.
[60] M. Pierantoni, I.Silva Barreto, M. Hammerman, L. Verhoeven, E. Törnquist, V. Novak, R. Mokso, P. Eliasson, H. Isaksson, A quality optimization approach to image Achilles tendon microstructure by phase-contrast enhanced synchrotron micro-tomography, Sci. Rep. 11 (2021) 1–14.
[61] S. Thomopoulos, J.P. Marquez, B. Weinberger, V. Birman, G.M. Genin, Collagen fiber orientation at the tendon to bone insertion and its influence on stress concentrations, J. Biomech. 39 (2006) 1842–1851.
[62] D. Qu, S.D. Subramony, A.L. Boskey, N. Pleshko, S.B. Doty, H.H. Lu, Compositional mapping of the mature anterior cruciate ligament-to-bone insertion, J. Orthop. Res. 35 (2017) 2513–2523.
[63] L. Zhang, S.P. Lake, V.K. Lai, C.R. Picu, V.H. Barocas, M.S. Shephard, A coupled fiber-matrix model demonstrates highly inhomogeneous microstructural interactions in soft tissues under tensile load, J. Biomech. Eng. 135 (2013) 011008.
[64] A. Faingold, S.R. Cohen, R. Shahar, S. Weiner, L. Rapoport, H.D. Wagner, The effect of hydration on mechanical anisotropy, topography and fibril organization of the osteonal lamellae, J. Biomech. 47 (2014) 367–372.
[65] A.G. Reisinger, D.H. Pahr, P.K. Zysset, Principal stiffness orientation and degree of anisotropy of human osteons based on nanoindentation in three distinct planes, J. Mech. Behav. Biomed. Mater. 4 (2011) 2113–2127.
[66] D. Carnelli, P. Vena, M. Dao, C. Ortiz, R. Contro, Orientation and size-dependent mechanical modulation within individual secondary osteons in cortical bone tissue, J. R. Soc. Interface 10 (2013) 20120953.
[67] K.L. Moffat, W.-H.S. Sun, P.E. Pena, N.O. Chahine, S.B. Doty, G.A. Ateshian, C.T. Hung, H.H. Lu, Characterization of the structure–function relationship at the ligament-to-bone interface, Proc. Natl. Acad. Sci. 105 (2008) 7947–7952.
[68] A.C. Deymier-Black, J.D. Pasteris, G.M. Genin, S. Thomopoulos, Allometry of the tendon enthesis: mechanisms of load transfer between tendon and bone, J. Biomech. Eng. 137 (2015) 111005–111005.
[69] A.C. Deymier, Y. An, J.J. Boyle, A.G. Schwartz, V. Birman, G.M. Genin, S. Thomopoulos, A.H. Barber, Micro-mechanical properties of the tendon-to-bone attachment, Acta Biomater. 56 (2017) 25–35.
[70] A.C. Deymier, A.G. Schwartz, Z. Cai, T.L. Daulton, J.D. Pasteris, G.M. Genin, S. Thomopoulos, The multiscale structural and mechanical effects of mouse supraspinatus muscle unloading on the mature enthesis, Acta Biomater. 83 (2019) 302–313.
[71] G.M. Genin, A. Kent, V. Birman, B. Wopenka, J.D. Pasteris, P.J. Marquez, S. Thomopoulos, Functional grading of mineral and collagen in the attachment of tendon to bone, Biophys. J. 97 (2009) 976–985.
[72] A. Aghaei, N. Bochud, G. Rosi, S. Naili, Assessing the effective elastic properties of the tendon-to-bone insertion: a multiscale modeling approach, Biomech. Model. Mechanobiol. 20 (2021) 433–448.
[73] L.J. Smith, A.C. Deymier, J.J. Boyle, Z. Li, S.W. Linderman, J.D. Pasteris, Y. Xia, G.M. Genin, S. Thomopoulos, Tunability of collagen matrix mechanical properties via multiple modes of mineralization, Interface Focus 6 (2016) 20150070.
[74] Y. Liu, S. Thomopoulos, C. Chen, V. Birman, M.J. Buehler, G.M. Genin, Modelling the mechanics of partially mineralized collagen fibrils, fibres and tissue, J. R. Soc. Interface 11 (2013) 20130835–20130835.
[75] Y. Liu, V. Birman, C. Chen, S. Thomopoulos, G.M. Genin, Mechanisms of Bimaterial Attachment at the Interface of Tendon to Bone, J. Eng. Mater. Technol. 133 (2011).
[76] W. Wagermaier, K. Klaushofer, P. Fratzl, Fragility of bone material controlled by internal interfaces, Calcif. Tissue Int. 97 (2015) 201–212.

[77] A.M. Torres, J.B. Matheny, T.M. Keaveny, D. Taylor, C.M. Rimnac, C.J. Hernandez, Material heterogeneity in cancellous bone promotes deformation recovery after mechanical failure, Proc. Natl. Acad. Sci. 113 (2016) 2892–2897.

[78] N. Rodriguez-Florez, M.L. Oyen, S.J. Shefelbine, Insight into differences in nanoindentation properties of bone, J. Mech. Behav. Biomed. Mater. 18 (2013) 90–99.

[79] S. Hengsberger, A. Kulik, P.H. Zysset, Nanoindentation discriminates the elastic properties of individual human bone lamellae under dry and physiological conditions, Bone 30 (2002) 178–184.

[80] I. Zlotnikov, E. Zolotoyabko, P. Fratzl, Nano-scale modulus mapping of biological composite materials: theory and practice, Prog. Mater Sci. 87 (2017) 292–320.

[81] R. LaComb, O. Nadiarnykh, S.S. Townsend, P.J. Campagnola, Phase matching considerations in second harmonic generation from tissues: effects on emission directionality, conversion efficiency and observed morphology, Opt. Commun. 281 (2008) 1823–1832.

[82] K.E. Stockhausen, M. Qwamizadeh, E.M. Wölfel, H. Hemmatian, I.A.K. Fiedler, S. Flenner, E. Longo, M. Amling, I. Greving, R.O. Ritchie, F.N. Schmidt, B. Busse, Collagen fiber orientation is coupled with specific nano-compositional patterns in *dark* and *bright* osteons modulating their biomechanical properties, ACS Nano 15 (2021) 455–467.

[83] M.L. Killian, L. Cavinatto, L.M. Galatz, S. Thomopoulos, The role of mechanobiology in tendon healing, J. Shoulder Elbow Surg. 21 (2012) 228–237.